Europium–palladium intermetallic thin layers

2008 J. Phys.: Condens. Matter 20 315006

(http://iopscience.iop.org/0953-8984/20/31/315006)

J. Phys.: Condens. Matter **20** (2008) 315006 (13pp) doi:10.1088/0953-8984/20/31/315006

Europium–palladium intermetallic thin layers

Paweł Maślankiewicz[1,2,3], Zbigniew Celinski[2] and Jacek Szade[1]

[1] Department of Solid State Physics, August Chełkowski Institute of Physics, University of Silesia, ul Uniwersytecka 4, PL-40-007 Katowice, Poland
[2] Center for Magnetism and Magnetic Nanostructures, University of Colorado at Colorado Springs, 1420 Austin Bluffs Parkway, Colorado Springs, CO 80918, USA

E-mail: pmaslank@us.edu.pl

Received 29 January 2008, in final form 5 May 2008
Published 26 June 2008
Online at stacks.iop.org/JPhysCM/20/315006

Abstract
Ultrathin films (8–41 Å thick) of $EuPd_3$ were grown using a molecular beam epitaxy system. Two approaches were used to create these layers: co-evaporation from elemental sources at elevated temperature on MgO(001) substrates and deposition of Eu–Pd layers on MgO(001) substrates and Fe(001) templates followed by their reaction. Growth on MgO at elevated temperature or post-growth annealing leads to island formation. The reaction of europium and palladium deposited on Fe(001) occurs at room temperature. Alloy formation was confirmed by reflection high energy electron diffraction, x-ray photoelectron spectroscopy and ferromagnetic resonance studies. A surface valence transition of europium in $EuPd_3$ thin films was observed and found to decrease with decreasing $EuPd_3$ thickness.

(Some figures in this article are in colour only in the electronic version)

1. Introduction

Europium belongs to the group of anomalous rare earths; it may exist in two valence states, Eu^{2+} or Eu^{3+}. Metallic europium is divalent. Europium in alloys or intermetallic compounds may be in a divalent, trivalent or intermediate-valent state [1]. In the case of europium intermetallic compounds containing Eu^{3+} ions in the bulk material, it was shown that a surface valence transition to Eu^{2+} occurs [2], and the outermost layers contain Eu^{2+} ions. This is the case, for example, for $EuPd_3$, $EuPd_5$ [3], $EuNi_5$, $EuPt_5$ [4] etc. The most thoroughly studied compound belonging to this group of europium intermetallics is $EuPd_3$, which has high chemical stability, indicated by its congruent melting at 1425 °C [5]. $EuPd_3$ was also observed to form as a surface compound for annealed europium layers deposited on polycrystalline palladium [6, 7] or Pd(111) single crystals [8–10].

Studies on europium layers deposited on bulk palladium indicate that the europium valence depends on the Eu layer thickness [6, 8, 9, 11, 12]. Moreover, the Eu^{2+}/Eu^{3+} ratio characterizing the surface valence transition seems to differ between $EuPd_3$ and $EuPd_5$ [3] and between thin-film $EuPd_3$(111)/Pd(111) and bulk $EuPd_3$ [8, 9]. This suggests that the europium valence in an ultrathin film may differ from that in the bulk compound of the same stoichiometry. However, europium–palladium intermetallics in the form of thin films of a predefined stoichiometry were not previously studied, thus inspiring this work, to study ultrathin $EuPd_3$ films and, in particular, europium valence as a function of film thickness.

The mixed valence of Eu is directly related to its magnetism. Eu^{3+} is non-magnetic ($J = 0$) according to Hund's rules. In contrast, Eu^{2+} has a large pure spin moment ($J = 7/2$). Thus controlling the valence state means controlling the magnetic moment. The possibility of switching between the non-magnetic trivalent and the magnetic divalent states could be interesting for future spintronic devices.

The aim of the present work is to investigate ultrathin films of $EuPd_3$ grown by molecular beam epitaxy. With this objective, growth and electronic properties studies of $EuPd_3$ layers on MgO(001) substrates and on Fe(001) templates were performed.

2. Experimental details

Ultrathin layers (8–41 Å thick) corresponding to the $EuPd_3$ composition were deposited using a molecular beam epitaxy

[3] Author to whom any correspondence should be addressed.

(MBE) system on MgO(001) substrates or on Fe(001) templates. These substrates were chosen because of their very different chemical properties on the one hand and the possibility of a good lattice match to $EuPd_3$ on the other hand. MgO crystallizes in the fcc lattice with $a = 4.211$ Å [13], Fe—in the bcc lattice with $a = 2.867$ Å ($a\sqrt{2} = 4.05$ Å) [14] and $EuPd_3$—in the sc lattice with $a = 4.09$ Å [15]. The polished surface of MgO(001) single crystals (SPI Supplies) was cleaned by outgassing in an ultrahigh vacuum at about 600–650 °C for 30 min. The Fe(001) template was grown either directly on a 4 × 6 reconstructed GaAs(001) substrate or on a Ag/Fe/GaAs(001) bilayer (∼750 Å silver, ∼ 6 Å iron), using one-side polished semi-insulating GaAs(001) wafers (American Xtal Technology, Inc). Deposition was performed by thermal evaporation of elemental sources (Eu (99.99%), Pd (99.99+%), Fe (99.99%), Ag (99.99%) and Au (99.999%)). Pressure in the vacuum chamber during deposition was typically in the 10^{-9}–10^{-8} Torr range (of which ∼90% was hydrogen; oxygen and water together formed less than 5%) and decreased to the 10^{-10} Torr range during subsequent XPS measurements. Residual gas composition was determined by residual gas analysis (using a Stanford Research Systems system, model RGA100). The deposition rate and deposited thickness were controlled by RHEED intensity oscillations and with a quartz monitor employing the z-match technique (Leybold Inficon Inc., model XTM/2) [16], using appropriate z-ratio corrections. For Ag, Au, Fe and Pd the tabulated values of z-ratios were used [16]. The z-ratio for europium ($z_{Eu} = 1.33$) was assessed using the formula [17]:

$$z = \sqrt{\frac{\rho_q \mu_q}{\rho_{Eu} \mu_{Eu}}},$$

where ρ_q and ρ_{Eu} are quartz and europium densities ($\rho_q = 2.648$ g cm^{-3} [18], $\rho_{Eu} = 5.244$ g cm^{-3} [19]) and μ_q and μ_{Eu} are the shear moduli ($\mu_q = 28.97$ GPa for AT-cut quartz used in deposition monitors based on quartz elastic constants given in [18]; $\mu_{Eu} \approx 8.3$ GPa as obtained by averaging data for polycrystalline europium from [20] and [21]). Pd and Eu rates or thicknesses necessary to obtain a desired $EuPd_3$ thickness were calculated using formulae [22]:

$$d_{Eu} = d_{EuPd_3} \frac{\rho_{EuPd_3}}{\rho_{Eu}} \frac{M_{Eu}}{M_{Eu} + 3M_{Pd}} \frac{1}{T_{Eu}},$$

$$d_{Pd} = d_{EuPd_3} \frac{\rho_{EuPd_3}}{\rho_{Pd}} \frac{3M_{Pd}}{M_{Eu} + 3M_{Pd}} \frac{1}{T_{Pd}}, \qquad \frac{r_{Eu}}{r_{Pd}} = \frac{d_{Eu}}{d_{Pd}}$$

with d_i being the thicknesses of i (i = Eu, Pd or $EuPd_3$), r_i—the deposition rates, T_i—the tooling ratios (close to 1 in the experimental configuration of the growth chamber used [23]), ρ_i—the densities ($\rho_{EuPd_3} = 11.45$ g cm^{-3} based on the crystallographic properties of $EuPd_3$ [15]) and M_i—the molar masses.

Further details concerning the growth system design are described in [23].

Reflection high energy electron diffraction (RHEED) studies were performed *in situ* using a 15 keV electron beam. An x-ray photoelectron spectroscopy system from Specs GmbH was used for *in situ* x-ray photoelectron spectroscopy (XPS) studies. Photoelectrons were excited with monochromatized Al Kα (1487 eV) and Ag Lα (2983 eV) radiation. A nine-channel hemispherical energy analyser (Specs GmbH, model PHOIBOS 150) was used for spectra acquisition. Strong charging effects were observed in some cases and a flood gun was used for sample neutralization during XPS measurements in those cases. Spectra were collected in normal and oblique (45°) photoemission, in an experimental configuration with the angle between the direction of the x-ray beam and the detector axis close to the so-called 'magic angle' (55°), for which photoemission asymmetry effects may be neglected [24]. The pass energy values used were 23.50 eV and 46.95 eV for Al Kα and Ag Lα radiation, respectively, corresponding to respective energy resolutions of 0.8 eV and 1.3 eV. After the XPS studies, the samples were capped with a 20 Å gold layer for subsequent *ex situ* ferromagnetic resonance (FMR) or atomic force microscopy (AFM) measurements. A K_u band spectrometer (24 GHz) employing a cylindrical cavity (TE_{011} mode) was used for the FMR investigations in the temperature range from 24 to 310 K. AFM studies were performed with an Omicron VT AFM XA 50/500 microscope in the contact mode at room temperature.

3. Experimental results

3.1. $EuPd_3$ layers grown on MgO(001)

The growth of $EuPd_3$ on MgO(001) was performed by two methods: (i) co-deposition from elemental sources at elevated temperature (475–500 °C) or (ii) successive deposition of palladium, europium and palladium layers with appropriate thicknesses followed by annealing. In both cases XPS studies indicate the formation of a Eu–Pd intermetallic compound by the chemical shift of the europium photoemission signal, which corresponds to Eu^{3+}, characteristic of palladium-rich Eu–Pd intermetallics (europium was found to be divalent in Eu_5Pd_2, Eu_3Pd_2, EuPd and $EuPd_2$ and trivalent in $EuPd_3$ and $EuPd_5$ [25–28]). For the Pd/Eu/Pd trilayer, the palladium layers were deposited both before and after europium deposition to increase the speed of intermixing of Eu and Pd (related to the number of interfaces) and to limit the interaction of the europium with residual gases in the vacuum chamber and with oxygen from MgO.

3.1.1. Growth mode and structural properties. The mode of growth of $EuPd_3$ on MgO(001) was investigated by RHEED, performed before and immediately after the deposition for all samples and additionally after annealing in the case of the samples obtained by the reaction of Pd/Eu/Pd trilayers. Selected RHEED patterns are presented in figure 1. The RHEED pattern changes with the thickness of the film for both types of samples. For low $EuPd_3$ coverage, polycrystalline rings with some texture are visible, corresponding to more or less randomly oriented grains. The rings disappear for thicker coverages and a large number of spots become visible. This kind of image may be analysed by the method described in appendix A. A comparison with figure A.1(g) of appendix A explains that the majority of spots visible in figures 1(e)–(j) are due to fcc(111) clusters. The remaining spots can be explained

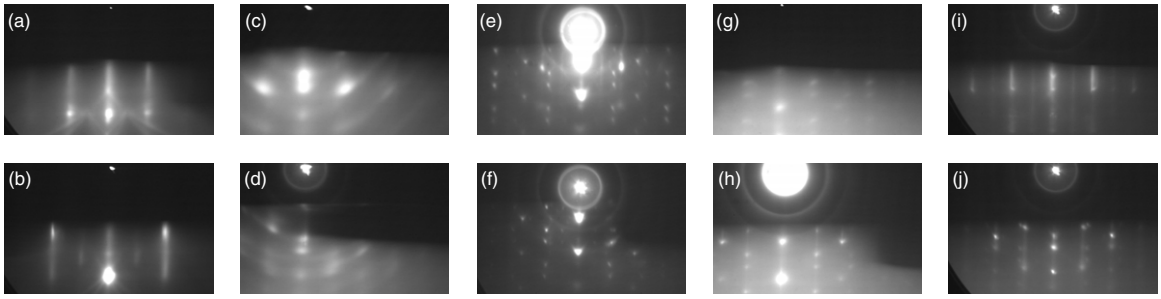

Figure 1. RHEED patterns for various $EuPd_3$/MgO(001) samples. (a) MgO, [100] azimuth; (b) MgO, [110] azimuth; (c) $EuPd_3$ (8 Å)/MgO obtained by Pd/Eu/Pd trilayer reaction, MgO [100] azimuth; (d) the same as (c), MgO [110] azimuth; (e) $EuPd_3$ (16 Å)/MgO obtained by co-deposition, MgO [100] azimuth; (f) the same as (e), MgO [110] azimuth; (g) $EuPd_3$ (21 Å)/MgO obtained by Pd/Eu/Pd trilayer reaction, MgO [100] azimuth; (h) the same as (g), MgO [110] azimuth; (i) $EuPd_3$ (41 Å)/MgO obtained by co-deposition, MgO [100] azimuth; (j) the same as (i), MgO [110] azimuth.

as belonging to three groups: (i) due to some additional orientations of the fcc(111) clusters, for example, using the notation explained in appendix A, for $[510]_{hex} \parallel x$ (such higher Miller-index directions give only spots fairly distant from the central line), (ii) due to a change of Bravais lattice type from fcc to sc (which would result for $EuPd_3$ in weak spots with horizontal distances from the central line at half the values for the main spots, the vertical distances being unchanged) and (iii) due to fcc(001) islands (analysed in a similar way as the (111) ones). An example of such a comparison is shown in figure 2.

From this analysis, the presence of (111) cubic islands rotated in-plane with respect to each other can be deduced. Moreover, this spotty image is almost unchanged by sample rotation around the z axis (figures 1(e)–(h)). This indicates that the (111) cubic islands have a nearly random in-plane orientation.

A difference is visible between the RHEED images for samples with $EuPd_3$ of nominal thicknesses of 21 and 41 Å (figures 1(g)–(j)). For the thicker $EuPd_3$ coverage, invariance of the island contribution to the RHEED pattern against rotation around the sample normal is no longer observed. Island-related spots are clearly visible only for the MgO[110] azimuth (figure 1(j)) but not so much for the MgO[100] one (figure 1(i)). This indicates that the (111) islands become in-plane oriented with increasing $EuPd_3$ coverage, most likely with $EuPd_3\langle 110\rangle$ (this is $\langle 100\rangle_{hex}$ using the notation from appendix A) parallel to MgO⟨110⟩. In addition to the disappearance of island-related spots, an increased intensity of the vertical lines is observed with increasing $EuPd_3$ thickness. These lines are related to the $EuPd_3$ (001)/MgO(001) epitaxy.

An analysis of the inter-spot and inter-line distances shows that the lattice parameters of the samples whose RHEED images are presented in figures 1(c) and (d), (e) and (f), (g) and (h) and (i) and (j) are 4.1(1) Å, 4.2(1) Å, 4.0(2) Å and 4.0(1) Å, respectively, and depend neither on the crystallographic direction nor on the cluster orientation within the experimental error. These values are close to the value for bulk $EuPd_3$ (4.09 Å) [15]. It should be, however, noted that additional spots due to the change of the Bravais lattice type from fcc to sc were not observed for the 21 Å thick sample obtained by Pd/Eu/Pd trilayer reaction at high temperature (figures 1(g) and (h)) (see also section 4).

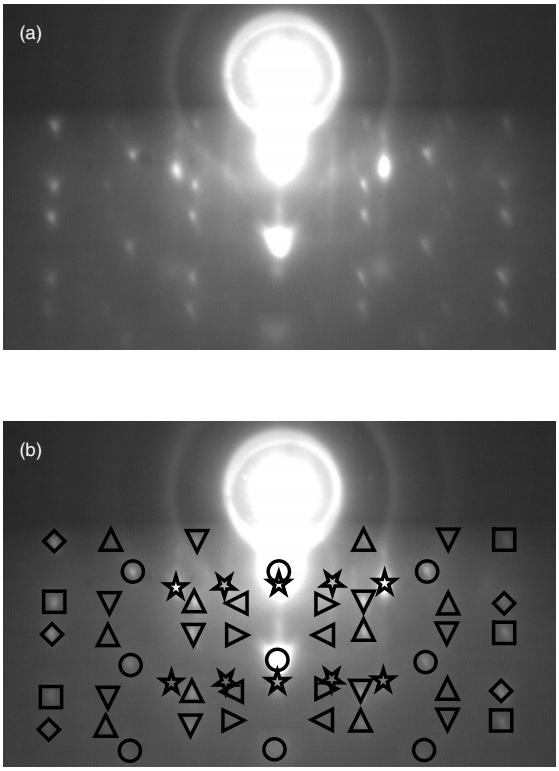

Figure 2. (a) Enlarged RHEED pattern for $EuPd_3$ (16 Å)/MgO obtained by co-deposition, MgO [100] azimuth (the same as presented in figure 1(e)), (b) the same pattern with symbols showing spots due to the same cluster orientation: fcc(111) clusters: ○—$\langle 100\rangle_{hex} \parallel x$ (x being the horizontal direction, as in figure A.1) and $\langle 110\rangle_{hex} \parallel x$, △—$\langle 210\rangle_{hex} \parallel x$, ▽—$\langle 120\rangle_{hex} \parallel x$, □—$\langle 510\rangle_{hex} \parallel x$ and $\langle 540\rangle_{hex} \parallel x$, ◇—$\langle 450\rangle_{hex} \parallel x$ and $\langle 150\rangle_{hex} \parallel x$; fcc (100) clusters: ☆—$\langle 100\rangle_{fcc} \parallel x$; ▷, ◁, ✲—selected weak spots due to the sc and not fcc Bravais lattice type of the clusters. Notation with triangular brackets ⟨⟩ is used to emphasize the equivalency of crystallographically equivalent in-plane directions (e.g. $[100]_{hex}$, $[010]_{hex}$ and $[\bar{1}10]_{hex}$ are equivalent and noted here simply by $\langle 100\rangle_{hex}$).

The analysis of the RHEED patterns for $EuPd_3$/MgO(001) suggests a Volmer–Weber type of growth [29]: isolated, randomly oriented clusters appear initially; they subsequently

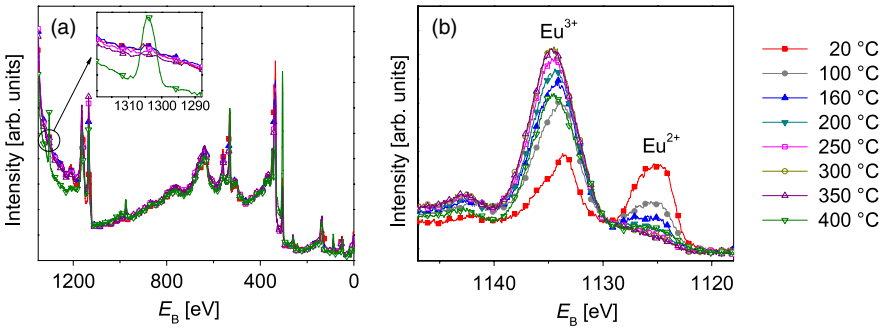

Figure 3. XPS spectra for a Pd (6 Å)/Eu (15 Å)/Pd (7 Å)/MgO(001) trilayer (21 Å $EuPd_3$ after reaction) acquired during annealing. (a) survey spectrum (inset: enlarged Mg 1s peak), (b) Eu $3d_{5/2}$ level. Selected experimental points at regular intervals are shown for reader's convenience.

become more (111)-textured; then this texture becomes more in-plane oriented and finally turns into (001) epitaxy.

Discontinuous island formation during growth at elevated temperature or extended annealing of Pd/Eu/Pd trilayers was also observed during XPS measurements, where it led to strong charging effects. These islands do not percolate and neutralization with a flood gun becomes necessary due to the highly insulating nature of the MgO substrate. Figure 3 shows XPS spectra taken during the annealing of a Pd (6 Å)/Eu (15 Å)/Pd (7 Å) trilayer (corresponding to 21 Å $EuPd_3$ (i.e. ∼5 atomic cells) after reaction between the layers). There are two main features visible in the Eu $3d_{5/2}$ spectrum, one at 1134 eV, corresponding to Eu^{3+} and another at 1126 eV, corresponding to Eu^{2+}. Some trivalent europium was present already at room temperature, which indicates europium–palladium intermixing leading to the formation of a palladium-rich alloy, in agreement with literature data on occurrence of intermixing between europium and palladium even at low temperatures [6–9, 11, 12]. The europium valence was found to exhibit a rapid increase with increasing temperature. (See also the discussion for $EuPd_3$ on Fe(001) in section 3.2.2.) No charging effects were observed until ∼350 °C, whereas strong charging occurred at ∼400 °C. Island formation at 400 °C was confirmed by the strong increase in intensity of the magnesium peaks, in particular of the Mg 1s peak at 1304 eV binding energy (183 eV kinetic energy). For a $EuPd_3$ layer $d = 21$ Å thick, the practical effective attenuation length for overlayer thickness measurements may be assessed with the help of the NIST database [30] to be EAL = 3.6 Å for 183 eV kinetic energy at normal electron emission, which would lead to an attenuation factor $e^{-d/(\mathrm{EAL}\cos 0^\circ)}$ of more than 300 (see appendix B for details). Therefore, the Mg 1s peak for the MgO substrate continuously covered by 21 Å of $EuPd_3$ should be hardly visible, which is in fact observed. In contrast to that, the Mg 1s peak for uncovered MgO should be well visible due to the high cross-section for Mg 1s photoionization [31] and that is the case for $EuPd_3$ layers on MgO after annealing at 400 °C.

To obtain more information about island formation of $EuPd_3$ on MgO(001), the sample for which XPS spectra are shown in figure 3 was subjected to *ex situ* atomic force microscopy experiments in the contact mode, performed after capping the sample with a protective Au layer (20 Å). Figure 4

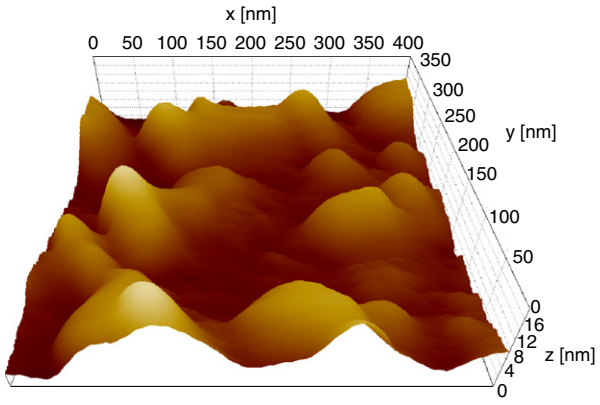

Figure 4. AFM picture (400 nm × 400 nm) of a 21 Å thick $EuPd_3$/MgO(001) sample obtained by reaction of Pd/Eu/Pd trilayer.

shows a 400 nm × 400 nm area of the sample. The root mean square (RMS) roughness of this area equals 30 Å, in contrast to the RMS value for bare MgO(001) of 0.8 Å. Large islands formed by Au-covered $EuPd_3$ are clearly visible. Their heights (referenced to the area between the islands) range from ∼50 to ∼140 Å and their lateral sizes from ∼300 to ∼2500 Å.

The fact that $EuPd_3$ initially forms islands on MgO instead of growing epitaxially is probably related to the well-known island formation by Pd on MgO (see, e.g., [32] for a review). This may be due to the similarity between the crystal structures of Pd and $EuPd_3$. Palladium crystallizes in the fcc structure with $a = 3.89$ Å [33], whereas $EuPd_3$ has a sc structure with $a = 4.09$ Å [15]. The sc lattice for $EuPd_3$ ($AuCu_3$ structure type) can be obtained from the fcc Pd lattice by replacing palladium atoms in the corners of the Pd unit cell by europium atoms.

3.1.2. Surface valence transition in $EuPd_3$/MgO(001). XPS investigations of the Eu 3d and 4d levels were performed to study the surface valence transition of europium in $EuPd_3$/MgO(001). Figure 5 shows the Eu $3d_{5/2}$ peak taken at normal and oblique (45°) emission with Al Kα radiation and at normal emission with Ag Lα radiation for a $EuPd_3$ film of nominal thickness of 41 Å (i.e. 10 unit cells) obtained by co-deposition on MgO(001) at ∼475 °C. This film, like all

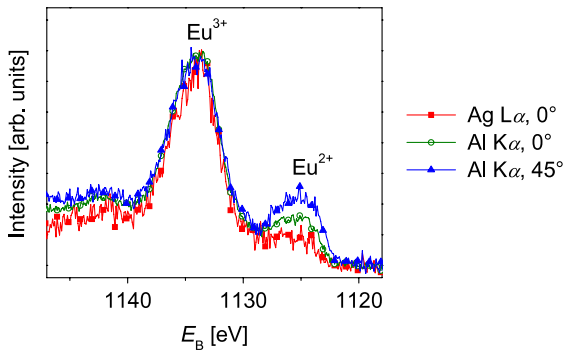

Figure 5. XPS spectrum of the Eu $3d_{5/2}$ level in different experimental configurations for a 41 Å thick $EuPd_3$/MgO(001) sample obtained by co-deposition at ∼475 °C. Angles listed are photoemission angles measured from sample normal. Every tenth experimental point is shown for reader's convenience.

the films deposited on MgO(001), had an island structure, which does not influence the conclusions presented here in a drastic way. The spectra presented in figure 5 were normalized to a constant peak area. The three experimental configurations considered in figure 5 correspond to different surface sensitivities, measured by different values of the mean escape depth (MED), as described in appendix B. As shown in figure 5, the intensity of the Eu^{2+} peak is smallest when MED = 13.7 Å (Ag Lα radiation at normal emission), is larger when MED = 5.2 Å (Al Kα radiation at normal emission) and is largest when MED = 3.8 Å (Al Kα radiation at emission at 45°). This clearly confirms the surface nature of the Eu^{2+} peak and thus the surface valence transition.

Table 1 lists the Eu^{2+}/Eu^{3+} ratios obtained from the Eu $3d_{5/2}$ spectra for samples of different nominal thicknesses. These ratios were determined from curve fitting the three visible components: the small satellite Eu^{3+} peak at 1142 eV, the main Eu^{3+} peak at 1134 eV and the Eu^{2+} peak at 1126 eV (see figure 5). There is, in fact, a small contribution from a Eu^{2+} satellite peak overlapping with the main Eu^{3+} peak. The intensity of this peak was estimated to be ∼5% of the main Eu^{2+} peak and was taken into account when calculating the ratios listed in table 1.

The surface valence transition seems to disappear as the layer thickness is reduced, which is a little surprising at first glance. This effect cannot be stress-induced, because the lattice parameter of bulk $EuPd_3$ is smaller than that of MgO (a_{EuPd_3} = 4.09 Å < 4.211 Å = a_{MgO}) [13, 15]. This lattice mismatch should induce lattice expansion for smaller thicknesses of $EuPd_3$. The lattice expansion, in turn, would favour the Eu^{2+} state, because it has a larger size than Eu^{3+} [34]. However, this is the inverse of what was observed. An increase of the Eu^{2+}/Eu^{3+} ratio with increasing film thickness could also be explained by a higher surface-to-volume ratio, related to the shape of the $EuPd_3$ islands. However, this would mean that the surface-to-volume ratio would have to increase with the amount of $EuPd_3$, which in turn would suggest that the $EuPd_3$ island growth would be columnar, and this is not consistent with the AFM and RHEED measurements. Therefore, the decrease of the europium surface valence transition with decreasing layer thickness seems to be an inherent property of the thin-film form of $EuPd_3$. This would be in agreement with results of Bertran *et al* [8, 9], where a slightly smaller surface valence transition was observed for a $EuPd_3$(111)/Pd(111) sample than for bulk $EuPd_3$. A similar situation was also observed for EuF_3, where the europium surface valence transition disappeared for an ultrathin film when compared to more bulk-like systems [35].

It is also worth mentioning that a reversible increase of the Eu^{2+}/Eu^{3+} signal upon heating the 41 Å $EuPd_3$/MgO(001) sample to ∼400 °C was observed.

Table 1. Eu^{2+}/Eu^{3+} ratios obtained from the Eu $3d_{5/2}$ spectrum for some $EuPd_3$/MgO(001) samples grown by co-deposition at high temperature. The thicknesses listed are nominal thicknesses (i.e. assuming uniform coverage).

	Eu^{2+}/Eu^{3+} intensity ratio		
$EuPd_3$ thickness (Å)	Al Kα radiation, oblique emission (45°)	Al Kα radiation, normal emission	Ag Lα radiation, normal emission
16	0.14(1)	0.12(1)	0.08(1)
21	Not measured	0.19(2)	0.11(1)
41	0.38(2)	0.25(1)	0.15(1)

3.2. *$EuPd_3$ layers grown on Fe(001)*

$EuPd_3$ was grown on Fe(001) templates by the deposition of a Pd/Eu bilayer at room temperature. The europium layer was first deposited on the Fe template to limit possible intermixing of Pd and Fe [36]. It seems unlikely that europium would intermix with iron, since theoretical predictions indicate no mutual solubility of europium and iron [37, 38]. There is only one known intermetallic compound in the Eu–Fe system, $EuFe_2$ [39]. This compound is probably metastable since other groups failed in attempts to synthesize it [40, 41], and it was not predicted in theoretical studies of the Eu–Fe binary phase diagram [37]. A palladium layer of appropriate thickness was deposited after the europium deposition, which also protected the europium from interaction with the residual gases in the vacuum chamber before intermixing with palladium. The deposited layers were subsequently analysed by XPS as a function of time elapsed after deposition. The reaction of palladium and europium was observed at room temperature. These layers were not annealed to prevent possible intermixing with iron. A 20 Å thick gold capping layer was deposited after the complete reaction between the europium and palladium to provide sample protection for the *ex situ* studies.

3.2.1. Structural investigations. In the case of growth of an 8 Å layer of $EuPd_3$ on 17 Å Fe(001), single-crystalline-like RHEED patterns were obtained after deposition of Eu on Fe and of Pd on Eu, as seen in figure 6. After the complete reaction of the bilayer, a similar pattern was obtained (although the streaks observed were much more diffuse) and, finally, the same kind of pattern, this time with increased quality, was observed after the deposition of an additional 20 Å thick layer of gold (figures 6(a), (c), (e), (g) and (i)). With increasing

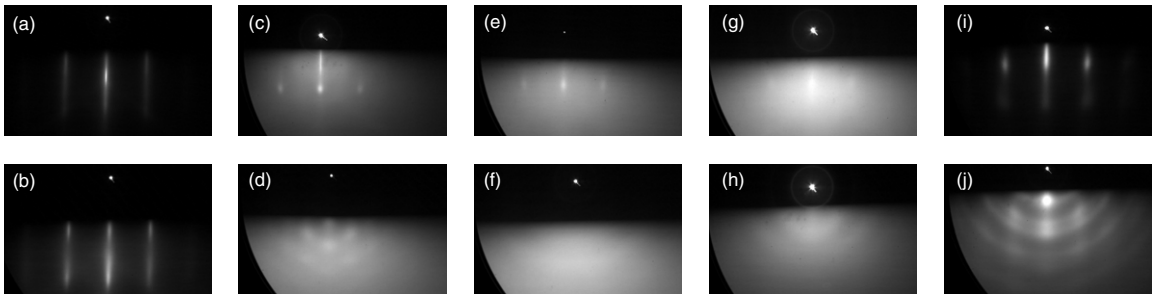

Figure 6. RHEED patterns acquired at various stages of growth of Pd–Eu samples on Fe(001). Images (a), (c), (e), (g) and (i) correspond to a Au (20 Å)/Pd (5 Å)/Eu (6 Å)/Fe (17 Å) sample (8 Å $EuPd_3$ after Eu–Pd reaction) and images (b), (d), (f), (h) and (j) correspond to a Au (20 Å)/Pd (13 Å)/Eu (15 Å)/Fe (21 Å) structure (21 Å $EuPd_3$ after Eu–Pd reaction). (a) and (b)—Fe(001) template, [110] azimuth; (c) and (d)—after Eu deposition, Fe [110] azimuth; (e) and (f)—after Pd deposition, same azimuth; (g) and (h)—after reaction of palladium and europium layers, same azimuth; (i) and (j)—after Au deposition, same azimuth.

$EuPd_3$ thickness, the RHEED pattern obtained after the Eu deposition became very diffuse and a new set of very broad spots appeared. The palladium pattern and that of the reacted $EuPd_3$ did not contain any spots or streaks, whereas some texture superposed on polycrystalline rings was obtained after growth of the gold capping layer (figures 6(b), (d), (f), (h) and (j)).

It is not straightforward to interpret the growth behaviour of Pd/Eu on Fe(001). The diffuse streaks observed for Eu (6 Å) on Fe(001) in the Fe [110] azimuth (figure 6(c)) correspond to the same inter-planar distance (2.07(4) Å) as that of pure Fe (2.05(3) Å) (figure 6(a)) within the precision of the measurement. A similar result is obtained for the Fe [100] azimuth, thus indicating a 1×1 pattern. A 1×1 overlayer with lattice parameter $\sqrt{2} \times 2.07$ Å $= 2.93$ Å is incompatible with the metallic radius of europium (2.04 Å) [19]. Epitaxial europium in any structure would have to form an overlayer on Fe(001) leading to fractional order streaks, which were not observed. This leads to a tentative suggestion that the streaks visible in figure 6(c) are not due to a Eu overlayer, but rather to the Fe template itself. This would mean that europium initially forms islands on Fe(001) and the streaks correspond to uncovered iron. There would be no pattern due to these europium clusters, either because they have very small sizes or because they are amorphous. The pure Fe(001) pattern contains elongated streaks with a slight modulation (figure 6(a)), which signifies a surface with a specific lateral ordering (terrace) length, shorter than the electron mean free path [42]. The pattern obtained after Eu coverage contains diffuse spots instead of the previous streaks, which indicates a shortening of the terrace length [42]. This may be explained by europium nucleation at characteristic points of the Fe(001) surface, for example at steps or kinks. With increasing europium coverage, the Eu clusters would then grow at the expense of the uncovered Fe terraces, thus reducing their size.

As it is typical for the Volmer–Weber growth mode, the Eu islands eventually coalesce with increasing europium deposits and form a continuous layer, and then a transformation to the bcc Eu structure growing in the (110) direction occurs. (It has been shown that europium of large thicknesses has a tendency to grow in the (110) direction, independently of substrate [43].)

Assuming the growth mode of Eu as described above, the RHEED patterns obtained after deposition of the remaining layers can be understood in the following way. For small europium coverage, leading to incomplete coalescence between Eu islands, palladium deposited after europium would form an overlayer both on the europium clusters and on the uncovered iron. This Pd overlayer would be epitaxial on Fe (it was demonstrated that Pd forms good quality overlayers on Fe(001) [44]), whereas it would be disordered on the Eu zones. The RHEED streaks (figure 6(e)) would then correspond to Pd/Fe epitaxial zones between Pd/Eu islands. The reaction of europium and palladium would then occur both perpendicularly to the Fe(001) plane and horizontally between europium islands and the neighbouring epitaxial palladium. This leads to an inhomogeneous reacted layer consisting of disordered zones giving the diffuse background of figure 6(g) and of epitaxial Pd:Eu zones in areas initially not covered by europium, resulting in hardly visible RHEED spots. Finally, the improvement of the RHEED pattern after the gold deposition (figure 6(i)) can be explained by gold epitaxial seeding on the Pd:Eu(001) areas and its growth in such a way that Au(001) layers also form above the disordered (Pd, Eu) areas. The formation of large Au(001) domains can be due to a stronger Au–Au interaction than the Au–(Pd, Eu) one.

The growth process is different if thicker Eu and Pd films are used. First, the europium deposition results in a uniform disordered Eu overlayer on the Fe template (figure 6(d)). The layer obtained after the Pd deposition is also more or less uniform (figure 6(f)). The reacted Eu–Pd film created a homogeneous but disordered overlayer on Fe (although there may have been some non-uniformity in the direction perpendicular to the Fe(001) surface) (figure 6(h)). Finally, the deposition of gold gave a polycrystalline Au film on the reacted $EuPd_3$ film (figure 6(j)). There was some texture visible for the gold overlayer, which is presumably due to a preferred Au(111) orientation.

This growth model is consistent with FMR results presented in section 3.2.3.

3.2.2. X-ray photoelectron spectroscopy study of the Eu–Pd reaction. As mentioned above, a reaction between europium and palladium was observed at room temperature. Figure 7

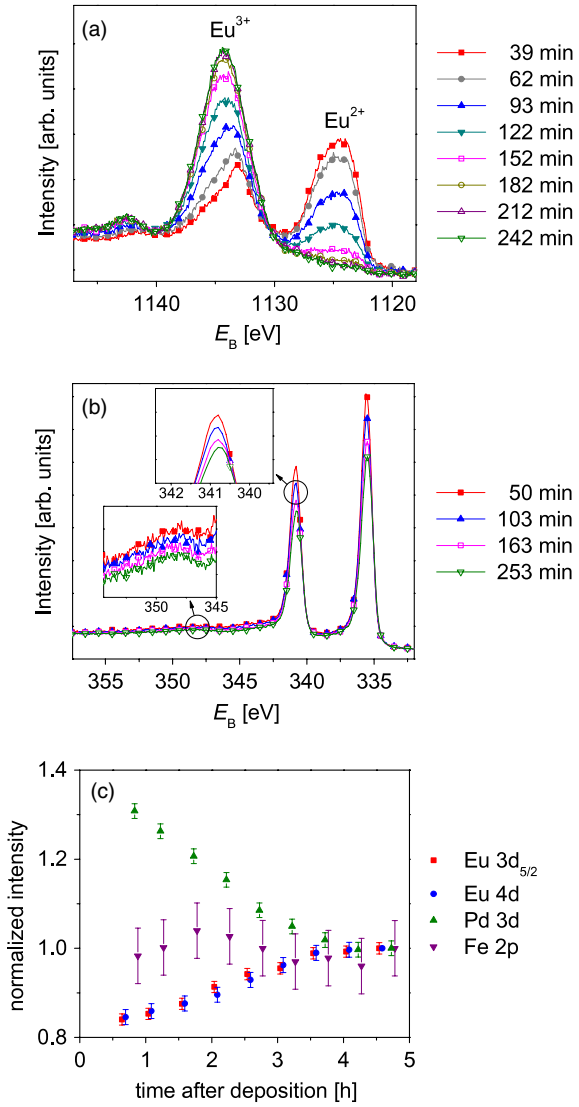

Figure 7. XPS spectra acquired as function of time for a Pd (13 Å)/Eu (15 Å)/Fe (21 Å) structure (corresponding to 21 Å $EuPd_3$). (a) Eu $3d_{5/2}$ level, (b) Pd 3d level, (c) changes in Eu $3d_{5/2}$, Eu 4d, Pd 3d and Fe 2p intensities, normalized to the final values.

shows a time-dependent XPS study of a Pd (13 Å)/Eu (15 Å) bilayer (corresponding to 21 Å $EuPd_3$, i.e. 5 unit cells). The reaction between europium and palladium is confirmed by the following observations.

(i) A significant change of europium valence. The change of europium valence could also be associated with sample degradation and the formation of Eu_2O_3, $Eu(OH)_3$ or a combination of the two compounds. To reject this possibility, the position of the Eu $3d_{5/2}$ peak of degraded europium deposited on iron and oxidized by long exposure to vacuum residual gases (∼31 h after deposition) was checked and it was observed that it has a maximum at a binding energy of 1134.7(1) eV, which is a higher value than in the case of the reacted Pd/Eu bilayer (1134.2(2) eV). (Literature data gives 1134.6 eV for Eu_2O_3 [45].) This chemical shift indicates that Eu^{3+} in our reacted Pd/Eu bilayer is primarily in metallic form and not in an oxidized one. A direct analysis of oxygen content based on XPS data is unfortunately impossible because both oxygen levels of known photoemission cross-sections [31] which could be used for quantitative analysis overlap with either a Pd or a Eu level. O 1s overlaps with Pd $3p_{3/2}$ and O 2s with Eu 5p. Due to the time necessary to achieve equilibrium (up to 4 h for a 21 Å thick $EuPd_3$ sample), it is possible that some sample degradation occurs and there is a contribution from europium oxide to the Eu^{3+} $3d_{5/2}$ signal at the high binding energy 'tail'. This degradation could eventually reduce the Eu^{2+} surface signal [46]. However, the Eu^{3+} $3d_{5/2}$ peak position indicates a dominant metallic character of trivalent europium in the reacted sample.

(ii) A slight change of the position of the Pd 3d line and a larger change of the position of its satellite line in the opposite direction, which accompany the change of europium valence, resulting in an increase in the main peak/satellite peak distance from 7.2(1) to 7.7(1) eV for the Pd $3d_{3/2}$ peak (the satellite for the Pd $3d_{5/2}$ peak overlaps with the main $3d_{3/2}$ line). This increase indicates a dilution of palladium in the sample [47], proving its intermixing with europium. An extensive analysis of the spread between the main peak and the satellite one was performed by Bertran *et al* [9] and the smallest spread was found for pure palladium when compared with different Eu–Pd intermetallics, in agreement with the general trend observed for various intermetallic palladium compounds [47].

(iii) A change of intensity of europium and palladium peaks with time. The intensity of the palladium 3d multiplet decreases with time and that of the Eu peaks increases (figure 7(c)), which is consistent with their intermixing. Some palladium atoms move further from the sample surface and therefore photoelectrons emitted from them are more likely to be scattered on their way out of the sample, which leads to the decrease of Pd peaks intensity. The inverse effect occurs for europium. The iron signal (coming from the Fe underlayer) is not changed, which indicates no intermixing of europium and palladium with iron.

Similar results are found for other thicknesses of the $EuPd_3$ films (8 and 12 Å).

3.2.3. Ferromagnetic resonance in iron for $EuPd_3$/Fe(001). An additional confirmation of the formation of a europium–palladium alloy is provided by an analysis of the ferromagnetic resonance spectra, which indicates different values of anisotropy for Fe films with a $EuPd_3$ interface when compared to Fe with other interfaces (Au, Pd).

Ferromagnetic resonance is a commonly used technique to study magnetic anisotropies in ultrathin ferromagnetic layers [48]. Measurements of the resonance field versus sample orientation and temperature allow, for example, the determination of the uniaxial out-of-plane anisotropy as a function of temperature [48]. An ultrathin Fe layer would exhibit different values of the uniaxial anisotropy due to different local environments of the Fe atoms at the interface. For example, if $EuPd_3$ or Pd layers were in contact with the Fe atoms at the interface, the resonance field should be different for the two structures, assuming the same thickness of the Fe layer.

Table 2. Four-fold in-plane effective anisotropy fields and effective demagnetizing fields for the two samples described in the text at room temperature (RT) and 24 K. $4\pi M_{\text{eff}}$ and $\frac{2K_{1\|}^{\text{eff}}}{M_S}$ values are given in kOe.

	Sample 1				Sample 2			
	$EuPd_3$ (21 Å)/Fe (21 Å)/Ag		Au/Fe (21 Å)/Ag		$EuPd_3$ (8 Å)/Fe (17 Å)/Ag		Pd/Fe (17 Å)/Ag	
	$4\pi M_{\text{eff}}$	$\frac{2K_{1\|}^{\text{eff}}}{M_S}$	$4\pi M_{\text{eff}}$	$\frac{2K_{1\|}^{\text{eff}}}{M_S}$	$4\pi M_{\text{eff}}$	$\frac{2K_{1\|}^{\text{eff}}}{M_S}$	$4\pi M_{\text{eff}}$	$\frac{2K_{1\|}^{\text{eff}}}{M_S}$
RT	16.3(2)	0.376(8)	15.4(2)	0.332(11)	15.5(2)	0.268(8)	17.1(2)	0.329(9)
24 K	16.3(2)	0.528(11)	15.9(2)	0.485(12)	16.6(2)	0.483(9)	17.0(2)	0.524(11)

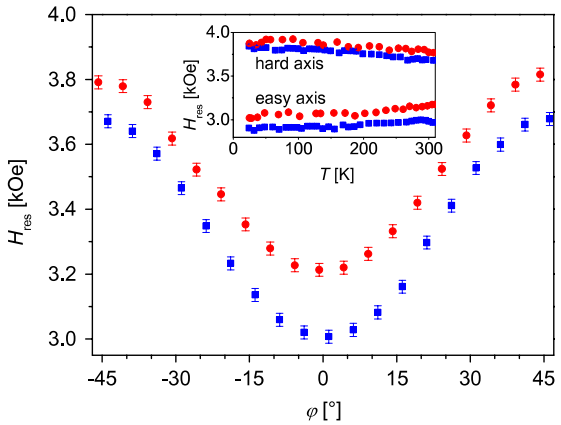

Figure 8. Angular dependence of the resonance field at room temperature for a Au (20 Å)/$EuPd_3$ (21 Å)/Fe (21 Å)/Ag(001) sample (■) and for a reference Au (20 Å)/Fe (21 Å)/Ag (001) sample (●). $\varphi = 0°$ corresponds to the Fe easy axis (the [100] direction). Inset: temperature dependence of resonance fields for the easy and hard axes for the Au (20 Å)/$EuPd_3$ (21 Å)/Fe (21 Å)/Ag(001) sample.

In order to study the ferromagnetic resonance properties of Fe(001) films covered by $EuPd_3$, samples with two zones were prepared on an Fe template layer. The first zone consisted of a Pd/Eu/Fe trilayer, while the second of a reference Fe layer only. Two samples were prepared this way. In the first sample, the first zone consisted of Au/$EuPd_3$ (21 Å)/Fe (21 Å)/Ag and the second zone of Au/Fe (21 Å)/Ag. The second sample had thinner $EuPd_3$ and Fe layers (Au/$EuPd_3$ (8 Å)/Fe (17 Å)/Ag) in the first zone and additionally a palladium layer in the second zone (Au/Pd (5 Å)/Fe (17 Å)/Ag).

The FMR measurements clearly indicate a difference between the resonance fields for the two zones of both samples. Figure 8 presents the angular dependence of the resonance field at room temperature and the inset shows the temperature dependence of the resonance field for the easy and hard axis of Fe for the two zones of the first sample described above ($f = 24$ GHz). The angular dependence clearly indicates a four-fold anisotropy of the single crystal Fe layer, it was thus fitted with the following formula [49]:

$$\left(\frac{2\pi f}{\gamma}\right)^2 = \left[H_{\text{res}} + 4\pi M_{\text{eff}} + \frac{K_{1\|}^{\text{eff}}}{2M_S}(3 + \cos(4\varphi))\right] \times \left[H_{\text{res}} + \frac{2K_{1\|}^{\text{eff}}}{M_S}\cos(4\varphi)\right],$$

where H_{res} is the resonance field for sample position at angle φ from the easy axis, $\frac{2K_{1\|}^{\text{eff}}}{M_S}$ is the four-fold in-plane effective anisotropy field, $4\pi M_{\text{eff}}$ is the effective demagnetizing field, f is the frequency of the microwaves used for the FMR measurements and $\gamma = g\frac{\mu_B}{\hbar}$ is the gyromagnetic ratio. For iron $\gamma = 18.4$ GHz kOe^{-1} based on the spectroscopic splitting factor value of $g = 2.09$ [50]. Results of the fits are presented in table 2.

The effective demagnetizing field, $4\pi M_{\text{eff}}$, is influenced by the uniaxial out-of-plane anisotropy and given by [48, 49]:

$$4\pi M_{\text{eff}} = 4\pi D M_S - \frac{2K_u^{\text{eff}}}{M_S} = 4\pi D M_S - \frac{2K_u}{M_S} - \frac{2K_u^s}{dM_S},$$

where D is the demagnetizing factor, M_S is the saturation magnetization, d is the thickness of the iron layer and K_u^{eff} is an effective uniaxial anisotropy constant, being the sum of two contributions, bulk K_u and interface $\frac{K_u^s}{d}$. The surface anisotropy constant K_u^s is a sum of constants for both interfaces of the thin Fe film, here for the Fe/Ag and $EuPd_3$ /Fe, Pd/Fe and Au/Fe interfaces.

These results clearly indicate that the two samples are characterized by different interface anisotropy properties due to the different overlayers ($EuPd_3$ versus Au for the first sample and $EuPd_3$ versus Pd for the second one).

Ferromagnetic resonance also allows the study of relaxation by measuring the linewidth of the absorption versus applied field. The absorption peak would be significantly broadened in the case of heterogeneous or non-uniform overlayers with an inhomogeneity range exceeding the exchange length $\delta = \sqrt{\frac{A}{2\pi M_S^2}}$ (A being the exchange stiffness coefficient), for iron $\delta = 33$ Å [48]. The results of the FMR linewidth measurements are collected in table 3. The resonance linewidth is similar for the two reference zones for both samples investigated despite different overlayers (Au/Fe/Ag versus Pd/Fe/Ag). However, there is a difference for the $EuPd_3$ zones. The first sample, with a thicker $EuPd_3$ overlayer (21 Å thick), has a significantly narrower line than the second one, with a thinner $EuPd_3$ film (8 Å thick). This suggests that the thicker $EuPd_3$ overlayer is more homogeneous than the thin $EuPd_3$ film, in agreement with the proposed growth mode of $EuPd_3$ on Fe(001) (section 3.2.1).

3.3. Discussion

Europium–palladium intermetallics have been grown on both MgO(001) substrates and Fe(001) underlayers and studied

Table 3. FMR linewidths (in kOe) at room temperature and 24 K. Values given correspond to the full width at half maximum of the Lorentzian resonance curve.

	Sample 1				Sample 2			
	$EuPd_3$ (21 Å)/ Fe (21 Å)/Ag		Au/Fe (21 Å)/Ag		$EuPd_3$ (8 Å)/ Fe (17 Å)/Ag		Pd/Fe (17 Å)/Ag	
	Easy axis	Hard axis	Easy axis	Hard axis	Easy axis	Hard axis	Easy axis	Hard axis
RT	0.14(2)	0.12(2)	0.16(1)	0.12(1)	0.26(2)	0.22(2)	0.15(2)	0.10(2)
24 K	0.16(2)	0.14(2)	0.26(2)	0.24(2)	0.36(4)	0.29(4)	0.19(4)	0.19(4)

using RHEED, XPS, AFM and FMR techniques. The rather fast Eu–Pd reaction may at first glance seem surprising in view of the relatively elevated liquidus temperature in the europium-transition metal phase diagrams; see, e.g., Eu–Ni [51], Eu–Rh [52], Eu–Pd [5], Eu–Pt [53]. In all these systems high melting point intermetallic compounds containing trivalent europium exist. Both bulk and surface diffusion for metals are known to depend on the melting point in the first approximation [54]. It has been demonstrated, however, that europium intermixes with palladium [6–9, 11, 12], rhodium [7] and silver [55] at room temperature. Some indications of intermixing with nickel and copper also exist [56]. Bertran *et al* indicated that europium–palladium intermixing occurs even at liquid nitrogen temperature [11]. This intermixing is at least partially due to the high reactivity of europium.

In previous studies of the Eu/Pd thin layer system, specific europium thicknesses were deposited on thick (bulk or bulk-like) palladium and the mixed interlayer formation was observed as function of Eu thickness. At room temperature some intermixing was observed beyond a critical europium coverage and attributed to the formation of an amorphous mixed layer [8, 9]. Annealing led to an increase of the Eu^{3+} signal [6–9, 11]. From combined x-ray diffraction and RHEED data it was determined that annealing of a Eu (190 Å)/Pd(111) sample at 800–1000 K led to the formation of an ordered epitaxial $EuPd_3$ film [9]. Similar results were also obtained by LEED [10]. This suggests that the mixed layer formed at room temperature is of a different nature than that obtained after annealing or that found after high temperature deposition. For those studies, the total Pd:Eu ratio was very large due to the very thick Pd substrate or template.

The difference between the investigations described here and the previous investigations [6–12] lies in the fact that in the present study the equilibrium stoichiometry of the layer formed is forced by the deposited ratio of Eu and Pd. Nevertheless, some similarities between the atomic arrangements in the reacted layers in the present case and in the case of the studies reported in [6–12] can be found.

Investigations on $EuPd_3$ formation on MgO(001) suggested the Volmer–Weber mode of growth, as described in section 3.1.1. Studies of Eu–Pd films produced by co-deposition clearly indicate the formation of ordered crystallites in the simple cubic $AuCu_3$ lattice type. The existence of crystallographic order between europium and palladium is confirmed by the appearance of spots or streaks which should be extinct in the face-centered cubic lattice (see section 3.1.1). The fact that a more epitaxial result is obtained for thicker $EuPd_3$ films may be explained by the longer total deposition time, which provides the initially nucleated clusters more opportunity for self-arrangement. In principle this self-arrangement could be accelerated by an increased substrate temperature during deposition, leading to faster diffusion. However the maximum substrate temperature was chosen to be ∼500 °C because europium vapour pressure becomes very significant at such temperatures and thus the sticking coefficient of europium may decrease dramatically. In the case of annealed Pd/Eu/Pd trilayers, the annealing was stopped once island formation was observed, well below the 475–500 °C used as the substrate temperature for the samples obtained by co-deposition. It was mentioned in section 3.1.1 that weak spots corresponding to the change of the Bravais lattice type from fcc to sc, observed for co-deposited samples, were not observed for annealed Pd/Eu/Pd trilayers. This can be explained by a lack of full crystallographic order between europium and palladium. This order could eventually occur upon further annealing. However, the presence of diffraction spots indicates crystalline nature of the layer. Crystallographic order in annealed Pd/Eu/Pd trilayers is worse than that in the co-deposited samples because of the lower temperature used, likely to result in an incomplete arrangement of Eu and Pd atoms in their respective sites (1a and 3c, using Wyckoff's notation) of the $EuPd_3$ lattice. Thus, co-deposition seems to result in samples of better quality (at least in relation to atomic arrangement) than annealing of the Pd/Eu/Pd trilayer.

The crystallographic analysis of the $EuPd_3$ samples deposited on iron is more complex. For thicker layers (corresponding to 12 and 21 Å of $EuPd_3$ deposited on iron), no single-crystalline RHEED pattern is observed. This is due to the mode of growth of europium on iron, which, in turn, leads to a non-epitaxial palladium overlayer and, therefore, to a $EuPd_3$ layer (after the intermixing of europium and palladium) which does not follow the iron registry. However, for an 8 Å thick $EuPd_3$ layer, some spots were observed which indicate an in-plane registry similar to that of pure iron (figure 6(g)). As mentioned in section 3.2.1, they were interpreted as Pd–Eu regions occurring by europium diffusion from Eu islands on Fe(001) into epitaxial Pd(001) overlayers on iron. For the simple cubic lattice of $EuPd_3$, additional streaks corresponding to the simple Bravais lattice type should be visible. These streaks were not observed, which may be due to their low intensity or to an at least partial disorder between europium and palladium in the $EuPd_3$ cell, leading to a situation close to the face-centered cubic Bravais lattice type (pure palladium crystallizes in the fcc structure [33]). This

result can be explained by the significant solubility of europium in palladium, exceeding 6% at room temperature [5]. (For bulk $EuPd_3$, a small solid solubility around the stoichiometric 1:3 composition was also suggested [27, 28].) In the case of ultrathin films, it is quite possible that this solubility range of europium in palladium is significantly extended, and $EuPd_3$ fits within this range. Annealing would then lead to crystallographic ordering between europium and palladium in the crystal lattice of $EuPd_3$ (if intermixing with the iron template layer does not occur), similar to the case of Eu/Pd(111) [8–10].

As described in section 3.2.1, the assumption that the weak streaks in the RHEED pattern for the 8 Å thick $EuPd_3$ layer (figure 6(g)) originate from single-crystalline Pd–Eu regions created by europium diffusion from Eu islands on Fe(001) into epitaxial Pd(001) overlayers on iron means that the diffuse background on RHEED patterns in figures 6(g) and (h) would be due to disordered parts of the sample where the europium–palladium reaction occurred on areas initially containing Pd overlayers over Eu deposited on iron. It would be interesting to address the question of whether this disordered zone is polycrystalline or amorphous. The RHEED patterns obtained are not sufficient to answer this question, because both a flat polycrystalline surface with very small grains and an amorphous one lead to diffuse RHEED patterns. It is usually believed that room temperature reactions between a europium overlayer and an underlayer of a different metal result in an amorphous mixed layer because the reaction temperature is much lower than the expected crystallization temperature [6, 7, 55]. However, the case of palladium could be exceptional, because there is a significant solubility of europium in palladium in the bulk, in contrast to other metals, for example silver, copper and nickel, for which no bulk M:Eu solid solutions exist [57–59]. It is thus possible that for Eu/Pd layers, crystalline solid solutions are formed by the reaction between the layers, which is considered competitive to formation of amorphous mixed layers [60]. The nature of the formed mixed layer depends on which situation would be energetically more favourable and possible to occur for thermodynamic reasons (to overcome the activation energy barrier of the transformation into the configuration in question).

The results of growth studies clearly indicate that the Eu–Pd mixed layer is formed on both MgO substrates and Fe templates. The formation of the alloy takes place even at room temperature but it is significantly accelerated at elevated temperatures. When the reaction takes place at low temperatures, the $EuPd_3$ layers are not ordered as in the bulk compound. The crystallographic order increases with increasing temperature.

4. Conclusions

$EuPd_3$ ultrathin layers were deposited by molecular beam epitaxy on MgO(001) and Fe(001) templates. A Volmer–Weber mode of growth occurs on MgO(001). There is a surface valence transition from Eu^{3+} to Eu^{2+} in $EuPd_3$. The Eu^{2+}/Eu^{3+} ratio decreases with decreasing layer thickness. Growth on Fe(001) by deposition of a Pd/Eu bilayer and its reaction at room temperature leads to formation of an alloy layer. Structural (RHEED) and ferromagnetic resonance studies suggest possible disorder between europium and palladium in $EuPd_3$/Fe(001).

Acknowledgments

Paweł Maślankiewicz acknowledges a scholarship from the Polish-US Fulbright Commission. The work at UCCS was supported by the National Science Foundation (grant DMR-0605629). Omicron scanning probe microscope used for AFM experiments was partly financed by the European Regional Development Fund (ERDF).

The authors would like to thank Caroline and Robert Camley for a careful reading of the manuscript.

Appendix A. Three-dimensional electron diffraction in small single-crystalline clusters

In three-dimensional x-ray diffraction from a single crystal which is thousands of atomic layers thick in all directions, the positions of the diffracted beams can be obtained by the Ewald construction. Due to the large number of atomic planes in real space, the corresponding nodes in reciprocal space are very small and thus they intersect the Ewald sphere only for very specific orientations of the crystal versus the incident beam. The real-space dimensions are much larger than the electron mean free path and thus preclude the observation of a three-dimensional electron diffraction pattern.

The situation is different for small single-crystalline clusters. The lateral dimensions for the clusters in the real space are now finite (for example, of the order of a few interatomic distances or some tens of interatomic distances). On the one hand, the three-dimensional electron diffraction becomes observable because the cluster size is comparable to the electron mean free path. On the other hand, the nodes in the reciprocal space are no longer point-like and have extended dimensions, the shape of these nodes is determined by the Fourier transform of the real-space cluster shape. Therefore for specific cluster orientations a number of them intersect the Ewald sphere and a set of regularly spaced spots is obtained in the diffraction pattern.

Figure A.1 shows the Ewald construction for fcc(111) clusters. For convenience, a hexagonal description of the fcc lattice (one of the two possible) is used, in a similar way as was performed for Eu/O-c (6×2) V(110) [61]. The z axis ($[001]_{hex}$, $[111]_{fcc}$) is defined as normal to the sample and the y axis as the incident beam azimuth. Systematic extinctions occurring for the fcc lattice lead to the disappearance of all reciprocal lattice nodes for which $2h + k + 2l \neq 3m$ (m being an integer), using the hexagonal (hkl) Miller indexes (figure A.1(a)). This is included by using three types of signs for the nodes, depending on the value of l modulo 3. The following parameters were used for the construction: fcc lattice parameter 4 Å, electron beam wavelength 0.1 Å, cluster size 14 Å. A diffraction spot is obtained whenever the Ewald sphere is intersected by a node. The size of the spots and their intensities are not evaluated.

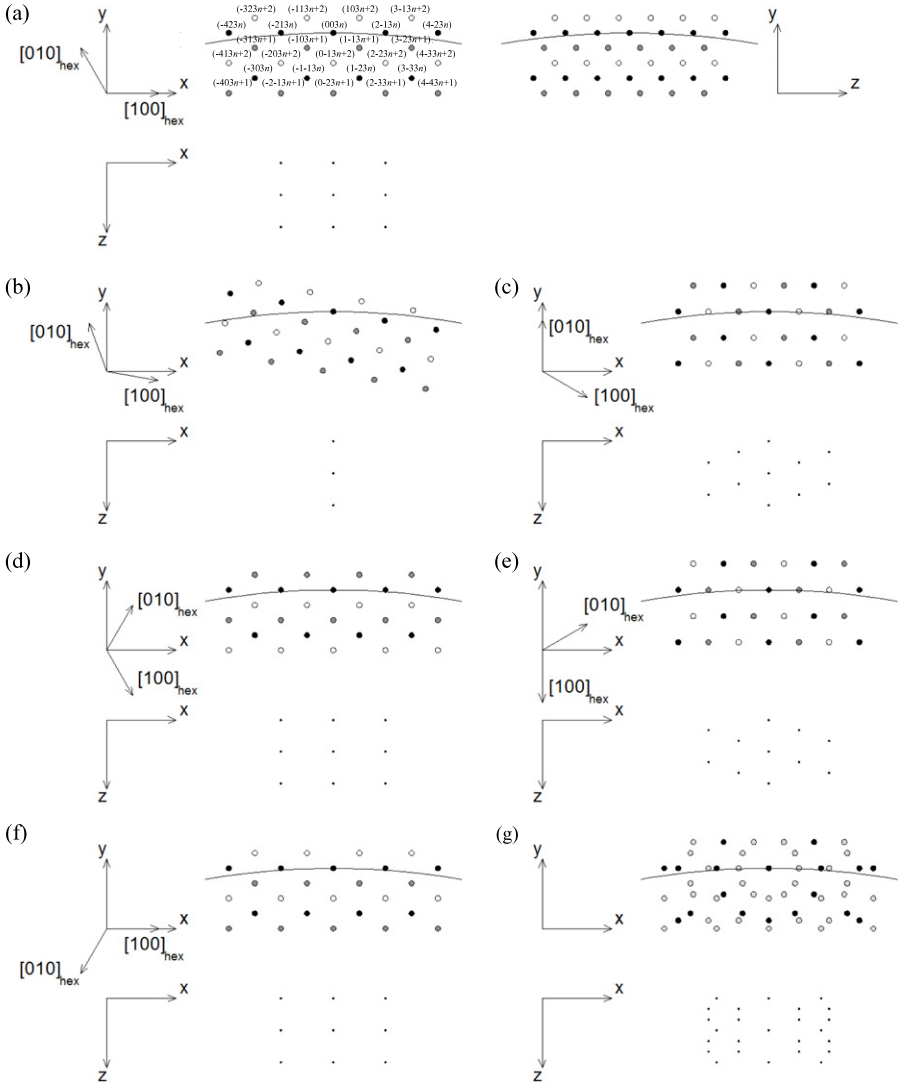

Figure A.1. Ewald construction for electron diffraction on fcc(111) islands. For each azimuthal position of the island, the top image presents the view perpendicular to the substrate surface ((x, y) plane) with the beam direction y positioned vertically, whereas the bottom image shows the corresponding RHEED pattern in the (z, x) plane. The (z, y) plane is also shown in the first configuration. (a) $[100]_{\mathrm{hex}} \parallel x$, (b) 10° off $[100]_{\mathrm{hex}} \parallel x$, (c) $[210]_{\mathrm{hex}} \parallel x$, (d) $[110]_{\mathrm{hex}} \parallel x$, (e) $[120]_{\mathrm{hex}} \parallel x$, (f) $[010]_{\mathrm{hex}} \parallel x$, (g) superposition of patterns for configurations (a), (c)–(e). Images (a)–(f): ●—nodes at $l = 3n$, ◉—nodes at $l = 3n + 1$, ○—nodes at $l = 3n + 2$. Image (g): ●—nodes at $l = 3n$, ◉—nodes at $l = 3n + 1$ and $l = 3n + 2$.

When $[100]_{\mathrm{hex}} \parallel x$, a spotty pattern is observed (figure A.1(a)). When the cluster is rotated around the z axis, all diffraction spots are quickly lost in the vicinity of the rotation axis apart from the spots on the axis, which are unchanged by the rotation (figure A.1(b)). A new set of spots is observed at $[210]_{\mathrm{hex}} \parallel x$, corresponding to a −30° rotation (figure A.1(c)). Further rotation again leads to an 'empty' pattern, and at $[110]_{\mathrm{hex}} \parallel x$ new spots are obtained (−60° rotation from the beginning), which coincide with the case $[100]_{\mathrm{hex}} \parallel x$ (figure A.1(d)). With further rotation, another image is obtained at $[120]_{\mathrm{hex}} \parallel x$ (−90° rotation from the beginning), being a mirror image to that for $[210]_{\mathrm{hex}} \parallel x$ (figure A.1(e)). Finally, rotation by −120° leads to a situation identical to the initial one due to the three-fold symmetry associated with the rotation axis parallel to the z direction (figure A.1(f)). A superposition of images from figures A.1(a), (c)–(e) is shown in figure A.1(g). This superposition corresponds to fcc(111) clusters oriented by a multiple of 30° with respect to each other when the beam is aligned along one of the low index directions ($[100]_{\mathrm{hex}}$, $[210]_{\mathrm{hex}}$ etc). Because of the extended size of the reciprocal lattice nodes, the same kind of image would be obtained for clusters with in-plane directions close to, but slightly different from those shown here ($[100]_{\mathrm{hex}} \parallel x$ etc) if they obey $[001]_{\mathrm{hex}} \parallel z$. A random in-plane orientation would require taking into account all possible rotations around the z axis and would give some additional spots distant from the rotation axis.

Appendix B. Substrate signal attenuation due to an overlayer and a measure of surface sensitivity for x-ray photoelectron spectroscopy

The various parameters describing electron intensity attenuation in electron spectroscopies due to scattering in solids were described in [62]. Two of them are used in the present analysis.

(i) The attenuation of the substrate signal due to an overlayer of thickness d equals $e^{-d/(\mathrm{EAL}\ \cos\theta)}$, where EAL is the practical effective attenuation length for overlayer thickness measurements and θ is the photoemission angle (measured from sample normal). EAL values can be calculated with the help of the NIST EAL database [30]. This database requires the following parameters for the calculation: the angles between the sample normal and the incident x-ray beam and between the sample normal and the detector axis, the photoemission asymmetry parameter (which can be neglected here because of the 'magic angle' experimental configuration (see section 2)), the kinetic energy of the photoelectrons emitted from the substrate, the chemical formula of the overlayer material and its band gap (0 eV for metals), density and number of valence electrons. For calculations of the EAL for the Mg 1s photoelectrons excited by Al Kα radiation (183 eV kinetic energy) emitted from $EuPd_3$-covered MgO (section 3.1.1), the density of $EuPd_3$ was assumed to equal $\rho_{EuPd_3} = 11.45$ g cm^{-3} (section 2) and the number of valence electrons to be $N_{V\ EuPd_3} = 39$, based on $N_{V\ Pd} = 10$ [62] and assuming $N_{V\ Eu^{3+}} = 9$ as for other trivalent lanthanides [62].

(ii) A convenient measure of the surface sensitivity for a specific experimental configuration with a specific electron kinetic energy is the mean escape depth (MED) [62]:

$$\mathrm{MED} = \frac{\int_0^\infty z\Phi(z,\theta)\,\mathrm{d}z}{\int_0^\infty \Phi(z,\theta)\,\mathrm{d}z},$$

where $\Phi(z,\theta)$ is the electron depth distribution function, z is the depth from the surface and θ is again the emission angle. In the case of an uncovered film of thickness d, all 'interesting' photoelectrons originate from the area between $z = 0$ and d, the MED then becomes:

$$\mathrm{MED} = \frac{\int_0^d z\Phi(z,\theta)\,\mathrm{d}z}{\int_0^d \Phi(z,\theta)\,\mathrm{d}z}.$$

MED values for $EuPd_3$ can be calculated with the help of the electron depth distribution function values provided by the NIST EAL database [30], using the same parameters for $EuPd_3$ as described above.

It should be noted that these parameters are slightly thickness-dependent due to the non-exponential photoelectron intensity attenuation with distance travelled [62].

References

[1] Miedema A R 1976 *J. Less-Common Met.* **46** 167
[2] Laubschat C 1998 *Magnetism and Electronic Correlations in Local-Moment Systems: Rare-Earth Elements and Compounds* ed M Donath, P A Dowben and W Nolting (Singapore: World Scientific) p 1
[3] Murgai V, Gupta L C, Parks R D, Mårtensson N and Reihl B 1982 *Valence Instabilities* ed P Wachter and H Boppart (Amsterdam: North-Holland) p 299
[4] Laubschat C, Perscheid B and Schneider W-D 1983 *Phys. Rev.* B **28** 4342
[5] Okamoto H 2003 *J. Phase Equilib.* **24** 197
[6] Selås T Ø and Raaen S 1990 *J. Phys.: Condens. Matter* **2** 7679
[7] Berg C, Raaen S and Ruckman M W 1992 *J. Phys.: Condens. Matter* **4** 4213
[8] Bertran F, Gourieux T, Krill G, Alnot M, Ehrhardt J J and Felsch W 1992 *Surf. Sci.* **269/270** 731
[9] Bertran F, Gourieux T, Krill G, Ravet-Krill M F, Alnot M, Ehrhardt J J and Felsch W 1992 *Phys. Rev.* B **46** 7829
[10] Wieling S, Molodtsov S L, Gantz Th, Hinarejos J J, Laubschat C and Richter M 1998 *Phys. Rev.* B **58** 13219
[11] Bertran F, Gourieux T, Krill G, Alnot M, Ehrhardt J J and Felsch W 1991 *Surf. Sci.* **245** L163
[12] Wieling S, Molodtsov S L, Gantz Th and Laubschat C 2001 *Phys. Rev.* B **64** 125424
[13] Villars P and Calvert L D 1991 *Pearson's Handbook of Crystallographic Data for Intermetallic Phases* 2nd edn, vol 4 (Materials Park, OH: ASM International) p 4296
[14] Villars P and Calvert L D 1991 *Pearson's Handbook of Crystallographic Data for Intermetallic Phases* 2nd edn, vol 3 (Materials Park, OH: ASM International) p 3213
[15] Villars P and Calvert L D 1991 *Pearson's Handbook of Crystallographic Data for Intermetallic Phases* 2nd edn, vol 3 (Materials Park, OH: ASM International) p 3196
[16] 1997 *XTM/2 Deposition Monitor, User Guide* Leybold Inficon
[17] Lu Ch-Sh and Lewis O 1972 *J. Appl. Phys.* **43** 4385
[18] Brice J C 1985 *Rev. Mod. Phys.* **57** 105
[19] Gschneidner K A Jr 2000 *CRC Handbook of Chemistry and Physics* 81st edn, ed D R Lide (Boca Raton: CRC Press) pp 4–114
[20] Burkhanov A M, Grazhdankina N P and Fakidov I G 1967 *Fiz. Tverd. Tela* **9** 748
Burkhanov A M, Grazhdankina N P and Fakidov I G 1967 *Sov. Phys.—Solid State* **9** 586 (Engl. Transl.)
[21] Rosen M 1968 *Phys. Rev.* **166** 561
[22] Huth M 2002 *Handbook of Thin Film Materials* vol 1, ed H S Nalwa (San Diego, CA: Academic) p 587
[23] Celinski Z 2001 *J. Vacuum Sci. Technol.* A **19** 383
[24] Seah M P 2003 *Surface Analysis by Auger and X-ray Photoelectron Spectroscopy* ed D Briggs and J T Grant (Chichester: IM Publications and SurfaceSpectra) p 345
[25] Harris I R and Raynor G V 1965 *J. Less-Common Met.* **9** 263
[26] Wickman H H, Wernick J H, Sherwood R C and Wagner C F 1968 *J. Phys. Chem. Solids* **29** 181
[27] Harris I R and Longworth G 1971 *J. Less-Common Met.* **23** 281
[28] Iandelli A and Palenzona A 1974 *J. Less-Common Met.* **38** 1
[29] Sree Harsha K S 2006 *Principles of Physical Vapor Deposition of Thin Films* (Amsterdam: Elsevier) p 685
[30] Powell C J and Jablonski A 2003 *NIST Electron Effective-Attenuation-Length Database—Version 1.1* (Gaithersburg, MD: National Institute of Standards and Technology)
[31] Scofield J H 1976 *J. Electron Spectrosc. Relat. Phenom.* **8** 129
[32] Henry C R 1998 *Surf. Sci. Rep.* **31** 231
[33] Villars P and Calvert L D 1991 *Pearson's Handbook of Crystallographic Data for Intermetallic Phases* 2nd edn, vol 4 (Materials Park, OH: ASM International) p 4905
[34] Shannon R D 1976 *Acta Crystallogr.* A **32** 751
[35] Burian W, Szade J, O'Keevan T and Celiński Z 2004 *Phys. Status Solidi* b **241** R15
[36] Budnik P S, Gordon R A and Crozier E D 2005 *Phys. Scr.* **T115** 495
[37] Predel B 1995 *Phase Equilibria, Crystallographic and Thermodynamic Data of Binary Alloys* (*Landolt-Börnstein, New Series* vol IV/5e) ed O Madelung (Berlin: Springer) p 111
[38] Ouyang Y, Zhong X and Tao X 2005 *Mater. Sci. Forum* **502** 57
[39] Ning Y-T, Zhou X-M, Zhen Y, Chen N-Y, Xu H and Zhu J-Zh 1989 *J. Less-Common Met.* **147** 167
[40] Moriarty J L, Humphreys J E, Gordon R O and Baenziger N C 1966 *Acta Crystallogr.* **21** 840

[41] Cannon J F, Robertson D L and Hall H T 1972 *Mater. Res. Bull.* **7** 5
[42] Korte U and Meyer-Ehmsen G 1990 *Vacuum* **41** 343
[43] Maeda A, Satake T, Fujimori T, Maeda Sh and Kuroda H 1990 *Thin Solid Films* **192** 135
[44] Celinski Z, Heinrich B, Cochran J F, Muir W B, Arrott A S and Kirschner J 1990 *Phys. Rev. Lett.* **65** 1156
[45] Teterin Yu A and Teterin A Yu 2002 *Usp. Khim.* **71** 403
Teterin Yu A and Teterin A Yu 2002 *Russ. Chem. Rev.* **71** 347 (Engl. Transl.)
[46] Mårtensson N, Hillebrecht F U and Sarma D D 1985 *Surf. Sci.* **152/153** 733
[47] Hillebrecht F U, Fuggle J C, Bennett P A, Zołnierek Z and Freiburg Ch 1983 *Phys. Rev.* B **27** 2179
[48] Heinrich B and Cochran J F 1993 *Adv. Phys.* **42** 523
[49] Heinrich B, Celinski Z, Cochran J F, Arrott A S and Myrtle K 1991 *J. Appl. Phys.* **70** 5769
[50] Stearns M B 1986 *Magnetic Properties of Metals* (*Landolt-Börnstein, New Series* vol III/19a) ed H P J Wijn (Berlin: Springer) p 85
[51] Predel B 1995 *Phase Equilibria, Crystallographic and Thermodynamic Data of Binary Alloys* (*Landolt-Börnstein, New Series* vol IV/5e) ed O Madelung (Berlin: Springer) p 123
[52] Palenzona A and Cirafici S 1998 *J. Phase Equilib.* **19** 162
[53] Predel B 1995 *Phase Equilibria, Crystallographic and Thermodynamic Data of Binary Alloys* (*Landolt-Börnstein, New Series* vol IV/5e) ed O Madelung (Berlin: Springer) p 128
[54] Flynn C P 2006 *J. Phys.: Condens. Matter* **18** S439
[55] Sørland G H and Raaen S 1993 *Physica* B **183** 415
[56] Passamani E C, Baggio-Saitovitch E, Mibu K and Shinjo T 1996 *Phys. Rev.* B **53** 6566
[57] Gschneidner K A Jr and Calderwood F W 1985 *Bull. Alloy Phase Diagr.* **6** 19
[58] Predel B 1994 *Phase Equilibria, Crystallographic and Thermodynamic Data of Binary Alloys* (*Landolt-Börnstein, New Series* vol IV/5d) ed O Madelung (Berlin: Springer) p 147
[59] Tung C H and Nash P 1989 *Bull. Alloy Phase Diagr.* **10** 127
[60] Liu B X, Lai W S and Zhang Z J 2001 *Adv. Phys.* **50** 367
[61] Gourieux T, Fréchard S, Dulot F, Eugène J, Kierren B and Malterre D 2000 *Phys. Rev.* B **62** 7502
[62] Tanuma Sh 2003 *Surface Analysis by Auger and X-ray Photoelectron Spectroscopy* ed D Briggs and J T Grant (Chichester: IM Publications and SurfaceSpectra) p 259